Geophysical Research Letters®

RESEARCH LETTER
10.1029/2023GL105946

Key Points:

- V_p/V_s values in the critical zone can be less than 1.4, suggesting a negative Poisson's ratio
- In near-surface environments, the assumption that materials have a positive Poisson ratio is not always justified
- Low V_p/V_s ratios may identify the onset of physical weathering in crystalline rock

Supporting Information:

Supporting Information may be found in the online version of this article.

Correspondence to:
B. A. Flinchum,
bflinch@clemson.edu

Citation:
Flinchum, B. A., Grana, D., Carr, B. J., Ravichandran, N., Eppinger, B., & Holbrook, W. S. (2024). Low V_p/V_s values as an indicator for fractures in the critical zone. *Geophysical Research Letters*, *51*, e2023GL105946. https://doi.org/10.1029/2023GL105946

Received 21 AUG 2023
Accepted 26 DEC 2023

Author Contributions:
Conceptualization: B. A. Flinchum, D. Grana, N. Ravichandran, B. Eppinger, W. S. Holbrook
Data curation: B. A. Flinchum, B. J. Carr
Formal analysis: B. A. Flinchum, B. J. Carr
Funding acquisition: B. A. Flinchum, D. Grana, B. J. Carr, W. S. Holbrook
Investigation: B. A. Flinchum, B. Eppinger
Methodology: B. A. Flinchum, D. Grana, B. J. Carr, N. Ravichandran, W. S. Holbrook
Project Administration: W. S. Holbrook
Resources: B. A. Flinchum, B. J. Carr, N. Ravichandran, B. Eppinger, W. S. Holbrook

Low V_p/V_s Values as an Indicator for Fractures in the Critical Zone

B. A. Flinchum[1], D. Grana[2], B. J. Carr[2], N. Ravichandran[1], B. Eppinger[3], and W. S. Holbrook[3]

[1]Environmental Engineering and Earth Science, Clemson University, Clemson, SC, USA, [2]Geology and Geophysics, University of Wyoming, Laramie, WY, USA, [3]Geosciences, Virginia Polytechnic Institute and State University, Blacksburg, VA, USA

Abstract Poisson's ratio for earth materials is usually assumed to be positive ($V_p/V_s > 1.4$). However, this assumption may not be valid in the critical zone because near Earth's surface effective pressures are low (<1 MPa), porosity has a wide range (0%–60%), there are significant texture changes (e.g., unconsolidated vs. fractured media), and saturation ranges from 0% to 100%. We present P-wave (V_p) and S-wave (V_s) velocities from seismic refraction profiles collected in weathered crystalline environments in South Carolina and Wyoming. Our data show that ∼20% of the subsurface has negative Poisson's ratios (V_p/V_s values < 1.4), a conclusion supported by borehole sonic logs. The low V_p/V_s values are confined to the fractured bedrock and saprolite. Our data support the hypothesis that weathering-generated microcracks can produce a negative Poisson's ratio and that V_p/V_s values can thus provide insight into important critical zone weathering processes.

Plain Language Summary When a material is squeezed, the ratio between the change in height and width is described by an elastic parameter called Poisson's ratio. Most earth materials have a positive Poisson ratio, meaning the material will expand when squeezed (e.g., Playdough or wet sand). Materials with a negative Poisson's ratio rarely occurs naturally and will shrink in all directions when squeezed. Cork is a common material with a Poisson's ratio of approximately zero. Cork is ideal for bottling wine because its width does not change when pushing it into the bottle's narrow neck. Here we use surface-based measurements to quantify Poisson's ratio from P-wave (Vp) and S-wave (vs.) velocities in the top 50 m of Earth's surface. Our results show an unexpected result—material in the CZ has a negative Poisson's ratio. We believe this unexpected behavior is caused by the combination of low effective pressures and small and irregular cracks created during rocks' transformation into soil. The cracks have a greater impact on the material's ability to resist compression. At the same time, most of the rock is still coherent and thus only experiences a minimal loss of shear strength.

1. Introduction

The structural development of the Earth's critical zone (CZ) is driven by physical and chemical weathering processes that transform bedrock into soil (Anderson et al., 2007; Brantley et al., 2017; Richter & Mobley, 2009). Weathering processes initiate below the surface, producing saprolite, weathered bedrock, and unweathered bedrock that can be tens of meters thick and hold clues about how physical and chemical weathering processes are affected by lithology (Bazilevskaya et al., 2013; Buss et al., 2017), fracture density (Lebedeva & Brantley, 2017, 2023; Molnar et al., 2007), foliation (Eppinger et al., 2021; Leone et al., 2020), regional and tectonic stresses (St. Clair et al., 2015), climate (Anderson et al., 2019; Chorover et al., 2011), and groundwater (Goodfellow et al., 2011; Rempe & Dietrich, 2014). In the last decade, P-wave velocities obtained by seismic refraction surveys have become common for characterizing the deep CZ over extensive areas (Befus et al., 2011; Donaldson et al., 2023; Holbrook et al., 2014; Uecker et al., 2023). Seismic velocities have been used to quantify volumetric strains under hillslopes (Hayes et al., 2019), estimate water holding capacity (Flinchum et al., 2018a; Holbrook et al., 2014; Klos et al., 2018), and highlight essential connections between CZ structure and drought resilience (Callahan et al., 2020, 2022).

Most CZ studies rely on P-wave velocity (V_p), but adding wave shear velocity (V_s) can provide additional information about water saturation and pressures in the CZ (Brantut & David, 2018; Prasad, 2002; Wang et al., 2012; Zimmer et al., 2002). The ratio between P-wave and S-wave velocities (V_p/V_s) can be used to calculate Poisson's

Validation: B. A. Flinchum
Visualization: B. A. Flinchum
Writing – original draft: B. A. Flinchum, D. Grana, B. J. Carr, B. Eppinger, W. S. Holbrook
Writing – review & editing: B. A. Flinchum, D. Grana, B. J. Carr, N. Ravichandran, B. Eppinger, W. S. Holbrook

ratio in elastic isotropic material (Flinchum et al., 2020; Pasquet et al., 2016). Unlike the other elastic moduli, Poisson's ratio (υ) does not require the density only the shear (G) and bulk (K) moduli (Equation 1):

$$\upsilon = \frac{3K - 2G}{2(3K + G)} = \frac{V_p^2 - 2V_s^2}{2\left(V_p^2 - V_s^2\right)} \tag{1}$$

Physically, Poisson's ratio describes a material's response to uniaxial stress. Defined as the negative ratio between transverse and axial strain, Poisson's ratio can range from −1.0 to 0.5, but most unsaturated Earth materials have values between 0.05 and 0.5 (Acuna et al., 2022; Baughman, 2003; e.g. Gercek, 2007; Greaves et al., 2011). Materials with negative Poisson's ratios are called auxetic and behave counterintuitively, collapsing inward on themselves under uniaxial compression (Acuna et al., 2022; Alderson & Alderson, 2007; Evans & Alderson, 2000; Ji et al., 2018, 2019). Materials with a Poisson's ratio of zero will have a V_p/V_s value of $\sqrt{2} \sim 1.4$ (Equation 1); V_p/V_s values less than 1.4 are uncommon in rocks and are treated with suspicion (Mavko et al., 2009).

Methods to estimate near-surface V_s are well established and include shear wave refraction surveys (Hunter et al., 2022; Liberty et al., 2022; Stümpel et al., 1984; Uhlemann et al., 2016) and multichannel analysis of surface waves (Park et al., 1999; Xia et al., 1999). However, co-located measurements of V_p and V_s for CZ applications remain rare. V_p/V_s values of near-surface materials (<100 m) often vary. There are observations of V_p/V_s values that fall within V_p/V_s of 1.6–1.8, but they seem to be the exception (Liberty et al., 2022; Uhlemann et al., 2016). Other observations report a larger-than-expected range, including high V_p/V_s values greater than 4 (Flinchum et al., 2020; Pasquet et al., 2015a; Stümpel et al., 1984) or even as high as 20 (Salas-Romero et al., 2021). There are reports of V_p/V_s values less than 1.4 in the CZ of Brazil (Trichandi et al., 2022), in dry soils (Salem, 2015), and in full waveform inversion results in the CZ of Pennsylvania (Liu et al., 2022). These observations raise an important question: what can anomalous V_p/V_s values tell us about physical and chemical processes that drive CZ evolution?

The CZ remains a seismically challenging place to work. It is one of the few places where a single profile (∼100–200 m long) can encounter a vast range in porosity (0%–60%), both fractured and porous media, a full range of saturation (0%–100%), and effective pressures near zero. Furthermore, it remains challenging to obtain high-quality samples that can be evaluated in existing laboratory settings at low effective pressures (<1 MPa). The notable lack of observational data means we do not fully understand the complex relationships between V_p, V_s, and CZ properties. Here, we present V_p and V_s data from three seismic refraction profiles spanning 523 m in weathered crystalline granitic bedrock. The profiles show that ∼20% of the subsurface has negative Poisson's ratios (V_p/V_s values < 1.4). Sonic-derived velocities from 12 nearby boreholes support this surprising observation. The low V_p/V_s values (<1.4) are confined to the saprolite and fractured bedrock and do not extend into the bedrock. We argue that weathering-induced microcracks create inelastic deformation that reduces the compressibility more than the shear strength. This results in larger decrease in P-wave velocity than S-wave velocity resulting in low V_p/V_s values. These values are possible because of the low effective pressures, and the small stresses and strains associated with seismic wave propagation in the CZ. Our results suggest that low V_p/V_s values could indicate the onset of weathering via microcracking in the CZ.

2. Site Selection

We investigated two sites on crystalline bedrock (Figure 1). The South Carolina Piedmont (SCP) site (436432E 3829851N Z17N) is in the Appalachian Piedmont and is underlain by igneous and metamorphic rocks (Pavich, 1989; Secor et al., 1986; Sherwood et al., 2010). The Blair Wallis (BW) site (327659E 3847004N Z13N) is on granitic rocks of the Sherman batholith, which has little to no foliation (Edwards & Frost, 2000; Eggler et al., 1969; Frost et al., 1999). Using a Voigt-Ruess-Hill mixing model (Hill, 1963), the mineralogical composition from published literature (Edwards & Frost, 2000; Frost et al., 1999; Holbrook et al., 2019), and elastic properties from Mavko et al. (2009) we calculated theoretical V_p, V_s, and V_p/V_s values of bedrock at each site (Supporting Information S1).

The SCP and BW sites have been well characterized with seismic refraction and drilling (Flinchum et al., 2018b; Holbrook et al., 2019; Keifer et al., 2019). We collected two V_p and V_s refraction profiles at SCP and one at BW. We collected the first SCP profile (SCP L1) in July 2021. We collected the second profile (SCP L2) in January 2023. SCP L2 crossed a borehole where we collected downhole sonic velocities (Figure 1). The BW site has been imaged with seven km of seismic refraction profiles (Flinchum et al., 2018a, 2018b), passive seismic surveys

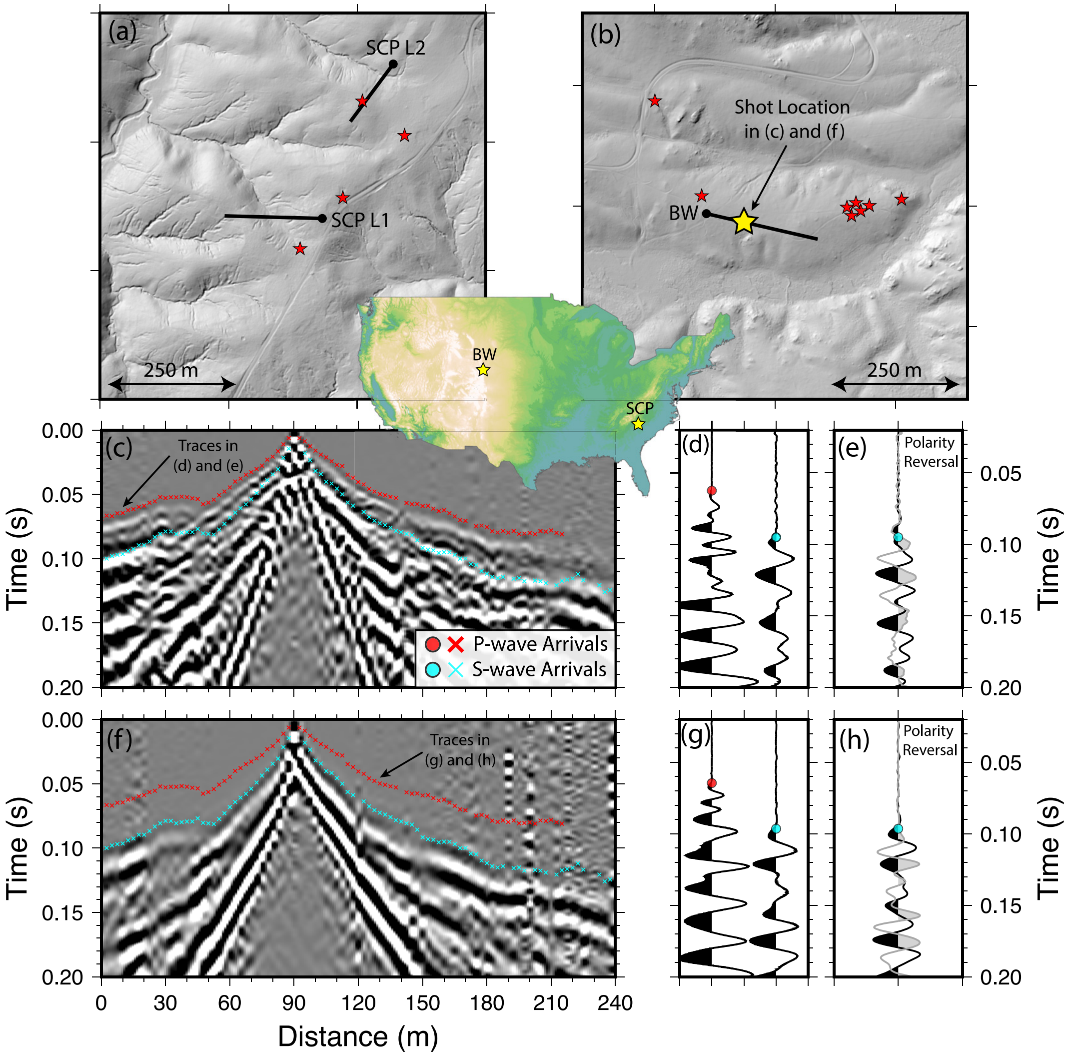

Figure 1. (a) Hillshade LiDAR map showing the two profiles and borehole locations for the South Carolina Piedmont (SCP) site. (b) Hillshade LIDAR map showing the BW profile and borehole locations. Shot gathers and traces in panels c–h are from BW. (c)–(h) Examples of our P-wave and S-wave picks and data from vertical and horizontal shots. The red symbols are the P-wave travel time picks, and the cyan symbols are the S_h-wave travel time picks. (c) Stacked shot gather using vertical geophones and vertical source. (d) Traces are from 10 m. The left trace is from the vertical shot gather (panel c) and the right trace is from the horizontal shot gather (panel f). (e) Pre-stacked traces from 10 m in the horizontal gather. The black trace represents the recording when swinging in direction 1 and the gray trace represents swinging in direction 2. The first arrival polarity is swapped indicating the S-wave arrival. When these two traces are subtracted it produces the second trace in panel d. (f) Stacked (by subtracting opposite direction swings) shot gather using horizontal geophones and the horizontal source. (g) Same as panel d but the traces are extracted from 130 m. The left trace is from the vertical shot gather (panel c) and the right trace is from the horizontal shot gather (panel f). (h) Same as panel e but for the trace at 130 m.

(Keifer et al., 2019; Wang et al., 2019), and surface and borehole nuclear magnetic resonance data (Flinchum et al., 2019; Ren et al., 2019). The rocks underlying the BW site are not foliated, but the saprolite shows a seismic anisotropy within the saprolite, interpreted as an inherited fracture fabric (Novitsky et al., 2018). There are nine boreholes at BW, and four at the SCP site (Figure 1).

3. Methods

3.1. Seismic Refraction

We collected V_p and V_s velocities using a sledgehammer source and 96 geophones. For V_p, we used a small aluminum plate as the source. We acquired V_s velocities using shear-wave refraction surveys (Hunter et al., 2022;

Pasquet et al., 2015b; Uhlemann et al., 2016) by inverting shear body wave travel times. We planted horizontal geophones (4.5 Hz) so that they would record ground motion perpendicular to the profile. We generated a horizontally polarized S-wave using a modified I-Beam source, striking each side of the I-beam. The subtraction of the two directional swings enhances shear arrivals and weakens P-wave arrivals (Figures 1c–1h). Shear wave refraction surveys exploit the decoupling of the SH wave from the P-SV system (Stein & Wysession, 2003). A description of the decoupling of SH waves from P-SV waves, information about the source, survey geometry, and analysis showing that our shear-wave refraction survey satisfies these conditions is provided in Supporting Information S1.

We trace-normalized the data and manually picked the first arrivals (Figures 1c–1h). P-wave arrivals were picked first and were plotted on the horizontal records to ensure accurate picking of the S-wave arrival (see Figure 1f). To invert the arrival times, we used the open-source Python Geophysical Inversion and Modeling Library (PyGIMLi) (Rücker et al., 2017), which is based on the shortest path algorithm (Moser, 1991; Rücker et al., 2017). The inversion uses a deterministic Gauss-Newton scheme to minimize χ^2, which requires a data weight for each pick. We assigned weights using a linear function of offset. We evaluated uncertainty by running the V_p and V_s inversion 200 times, randomly removing 20% of the travel time picks for each inversion to account for picking uncertainty. We quantified model uncertainty by starting each inversion with different starting velocity gradients and presenting the average of all 200 inversions. We used the inverted velocity models to compute synthetic seismograms using finite difference schemes that applied the elastic and acoustic wave equations (Juhlin, 1995; Stockwell, 1999). The Supporting Information S1 details data collection, picking, modeling, and uncertainty analysis.

3.2. Sonic Velocities

We acquired full waveform sonic data using a three-receiver, 2SAF-3R tool manufactured by Mount Sopris Instruments. We logged ∼340 vertical meters at nine boreholes at the BW site and ∼100 m at four boreholes at the SCP site. A subset of V_p sonic velocities at BW was reported in previous studies (Flinchum et al., 2018a, 2022). P- and S-wave velocities were determined from the three-receiver offsets using semblance, computed by summing the amplitudes along 15 different velocities over a 50 us window in WellCAD software version. 5.2 (ALT, https://www.alt.lu/). The highest semblance value was automatically picked across the entire log for both P-waves and the first shear phase. We inspected all semblance picks and manually adjusted sporadic picks. S-wave velocities in the sonic logs result from a converted wave caused by the strong elastic contrast between the surrounding rock and fluid (Haldorsen et al., 2006; Hornby & Murphy, 1987). Data were inverted using industry standards provided in WellCad.

4. Results

4.1. Seismic Refraction

The RMS error for all V_p and V_s models was under 2 ms (Figure 2). All picked travel times were fit within 7 ms, and the mean of the misfit was around zero (Figures S6–S8 in Supporting Information S1). We show contours for 1,200 ± 100 m/s and 4,000 ± 500 m/s as proxies for the boundary dividing saprolite and fractured rock and for the depth to bedrock in crystalline based on data presented in Flinchum et al. (2018b) and Holbrook et al. (2014). For the following analysis of the V_p/V_s models, we considered only the cells with at least one ray path from the V_p and V_s models.

General and consistent patterns emerge from the V_p/V_s values in the refraction profiles (Figure 2). The mean V_p/V_s value along SCP L2 is higher than SCP L1 (SCP L1 = 1.66 ± 0.004; SCP L2 = 1.71 ± 0.007; $p = 0.0$), but differences in the V_p/V_s value between SCP L2 and BW are negligible (1.66 ± 0.004 at SCP and 1.67 ± 0.006 at BW; $p = 0.64$). All three V_p/V_s models show a thin and consistent 1–2 m layer of higher V_p/V_s values at the surface that is required to fit the near-offset arrival times and is associated with low model uncertainty (Figure S5 in Supporting Information S1), which is likely caused by a change in pore shape. Beneath this layer, low V_p/V_s values can extend up to 40 m into the subsurface. In all three profiles, the low V_p/V_s values (<1.4) occur only in the saprolite or weathered/fractured bedrock (Figures 2c– 2f and 2i), above the 4,000 m/s V_p contour (Figure 2). We observe V_p/V_s values less than 1.4 at SCP L1 and BW when incorporating the uncertainty from the bootstrapping inversion scheme (Supporting Information S1). This suggests that V_p/V_s values less than 1.4 are resolvable and required to fit the data (Figures S9 and S10 in Supporting Information S1). At SCP L2, the probability of being less than 1.4 is reduced, suggesting that the V_p/V_s values on that profile might be low but not negative

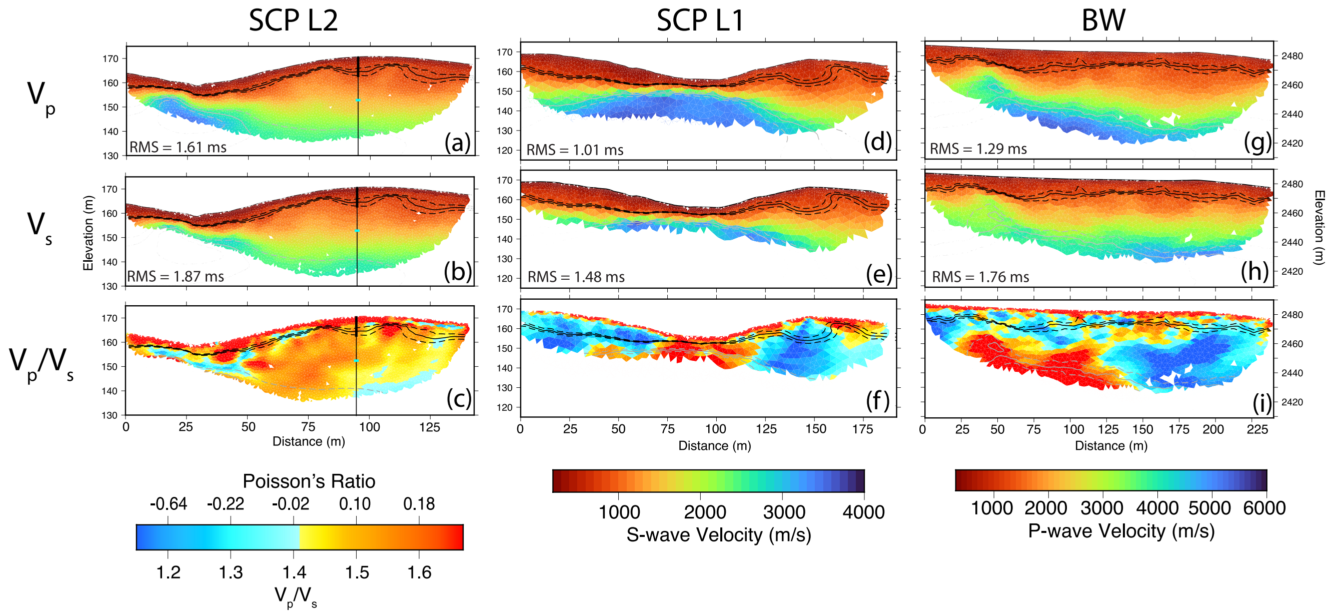

Figure 2. Seismic refraction results. The left column (a)–(c) are from SCP L2, the middle column (d)–(f) are from SCP L1, and the right column (g)–(i) are from BW. The top row (a, d, and g) are final V_p models masked by ray coverage with the RMS fits shown in the lower right-hand corner. The solid black contour is 1,200 m/s, and the dashed black contours are 1,100 and 1,300 m/s. The solid gray contour is 4,000 m/s while the dashed gray contours are 3,500 and 4,500 m/s. The V_s model results are the middle row (b, e, and h). The colormap has been rescaled, assuming a constant V_p/V_s value of 1.5. The velocity contours are from the V_p model. The bottom row is the V_p/V_s values. The colormap was chosen so that values with V_p/V_s values less than 1.4 ($\upsilon < 0$) are shown as cooler colors and V_p/V_s values greater than 1.4 ($\upsilon > 0$) are shown in warmer colors. Poisson's ratios are shown in the color scale using Equation 1.

(Figure S11 in Supporting Information S1) Thus, low V_p/V_s (<1.4), or at least very close to 1.4 values, must be present to explain our travel time observations.

4.2. Sonic Velocities

Sonic velocities from the wells at both sites show similar V_s ranges (Figure 3c), while at BW, V_p spans a wider range (~2,200–6,500 m/s). The distribution of V_s at both sites shows bimodal distributions, where the BW site has lower V_s velocities (Figure 3c). The larger variability in the distributions at BW results from including eight different wells. SCP only includes four wells. Despite the variability, there is a relatively linear relationship between V_p and V_s at both sites (Figure 3a). Most of the data at BW have V_p/V_s values of ~1.8 ($\upsilon = 0.28$), while the SCP appears to fall along a line closer to ~1.5 ($\upsilon = 0.10$) (Figure 3c). Probability density functions (PDF) of V_p/V_s values of the sonic logs from BW show a large peak (1.90 ± 0.002, mean ± standard error) and show only 2% of the data have negative Poisson's ratios ($V_p/V_s < 1.4$) (Figure 3d). The V_p/V_s PDF of the sonic velocities at SCP shows a much narrower peak with a mean and standard deviation of 1.49 ± 0.001, with 19% of the sonic V_p/V_s values falling below 1.4 (Figure 3d). The sonic velocities at BW have a much larger range of observed V_p/V_s values, suggesting more velocity heterogeneity at the BW site.

SCP L2 crosses a borehole at 95 m (Figure 1). The water level was 17.5 m bgs (Figures 2a–2c), and the casing depth is 8.8 m bgs. SCP L2 allows comparing the refraction V_p/V_s values to the sonic V_p/V_s values (Figures 3a and 3b). The sonic velocities are only available in fractured or fresh bedrock below the water table. The V_p and V_s profiles from SCP L2 are slower than the sonic velocities at almost all depths, but at greater depths (~25 m), the V_p and V_s velocities match the sonic velocities within uncertainty (Figure 3a). The mismatch between sonic and surface is common near the surface and could be caused by frequency differences which results in different averaging volumes (see Flinchum et al., 2022).

5. Discussion

The V_p/V_s values less than 1.4 observed in the surface refraction (Figure 2) and sonic logs (Figure 3) required additional scrutiny. Additional analysis described in Supporting Information S1 demonstrates that these values are not artifacts. First, we showed that the picked S-wave arrivals are refracted arrivals, not mode-converted waves.

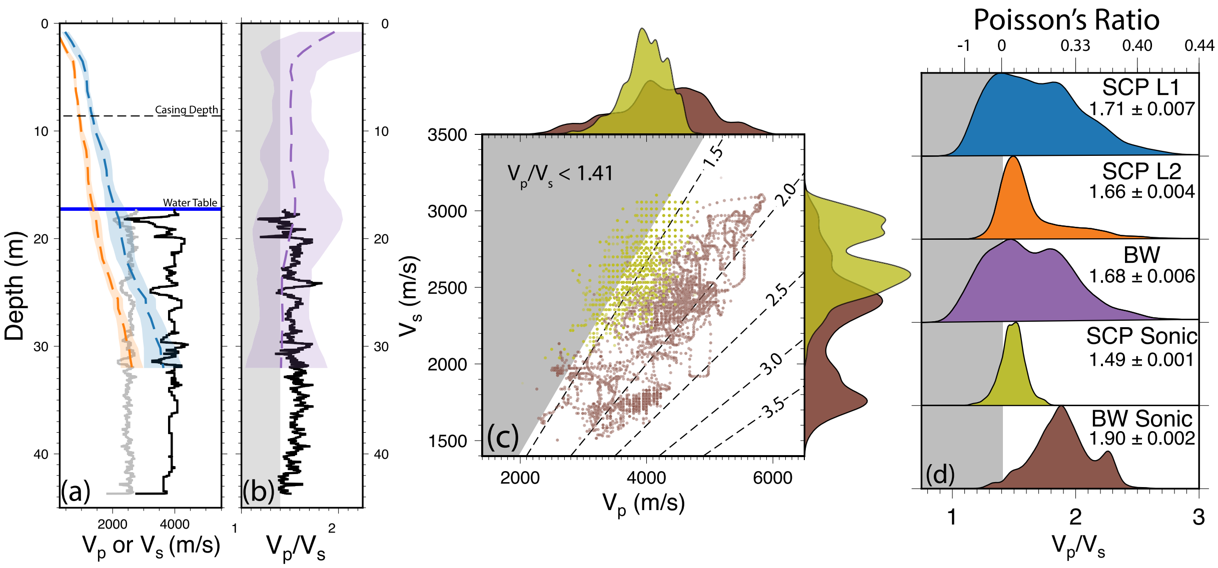

Figure 3. (a) A comparison of SCP L2 and the sonic velocity logs. The thin black line is the sonic V_p. The thin gray line is the sonic V_s. The dashed blue line and corresponding envelope are the extracted $V_p \pm 1\sigma$ (Figure S5 in Supporting Information S1). The dashed orange line and corresponding envelope are the extracted $V_s \pm 1\sigma$. The surface profiles only show where at least one ray passes through the V_p and V_s models. (b) The black curve is the V_p/V_s profile computed from the sonic logs. The dashed purple line is the V_p/V_s value extracted from the tomography model. The envelope is the uncertainty associated by taking the ratio using $(V_p + 1\sigma)/(V_s - 1\sigma)$ and $(V_p - 1\sigma)/(V_s + 1\sigma)$. (c) Sonic velocities, where V_s is plotted as a function of V_p for all available sonic logs. The yellow color is for SCP, and the brown color is for BW. Normalized Gaussian PDFs for V_s are shown on the right of the plot and V_p are plotted on top. Dashed lines are constant V_p/V_s values. (d) Normalized Gaussian PDFs of the distributions of V_p/V_s. Poisson's ratios are plotted on the top using Equation 1. The means and standard errors are reported in each plot. V_p/V_s values less than 1.4 ($\upsilon < 0$) are marked by a gray box.

Our acquisition geometry satisfies the conditions that allow SH waves to be decoupled from P-SV waves (Figures S1 and S2 in Supporting Information S1). Out-of-plane effects that create SH-P-SV coupling are unlikely because of the high amplitude and coherency of the SH arrivals (Figure S3 in Supporting Information S1). Because mode-converted waves might also have slow apparent velocities similar to those of the SH arrivals (Figure S4 in Supporting Information S1), we used a finite-difference code (Juhlin, 1995; Stockwell, 1999) to compute the elastic response of the BW profile (Figure 1b) to conclusively show that the picked arrivals are SH waves, not mode-converted waves (Mi et al., 2015), which arrive earlier (Figure S13 in Supporting Information S1).

Second, we tested our ability to resolve V_p/V_s values less than 1.4 by conducting uncertainty analysis (Figures S9–S11 in Supporting Information S1) and estimating the probabilities of V_p/V_s values less than 1.4 (Figure S9–S11 in Supporting Information S1). At SCP L1 and BW low V_p/V_s values over large regions are required to fit the observed data. At SCP L2, the probability is lower, and low V_p/V_s values are focused around a boundary at the valley bottom (Figure 2a). To determine if a higher V_p/V_s value of 1.5 would fit the data, we constructed S-wave velocity models by dividing the V_p models by 1.5 and tracing the rays (Figure S6–S8 in Supporting Information S1), which also shows that V_p/V_s values less than 1.4 must occur to fit our picked travel times (Figures S6–S8 in Supporting Information S1). The following discussion sections address the question: *is there an underlying mechanism that can create large regions of negative Poisson's ratios, and what implications do these values have concerning our understanding of deep CZ architecture?*

5.1. Low Effective Pressures and Irregularly Shaped Cracks

Negative Poisson's ratios in Earth materials were reported as early as the 1930s (Zisman, 1933) and are consistently reported in thermally cracked granites under uniaxial compression (Alm et al., 1985; Griffiths et al., 2018; Homand-Etienne & Houpert, 1989). Negative Poisson's ratios have also been reported for sedimentary rocks at low pressures (Li & Ji, 2021; Zaitsev et al., 2017a, 2017b). In thermally cracked granites, auxetic behavior appears after thermal cracking has occurred. These cracks create irregular crack geometry, which causes the material to rotate and collapse inward before any other deformation can occur (Potyondy & Cundall, 2004; Zhao, 2016; Zhao et al., 2020). The auxetic behavior disappears at confining pressures greater than 15 MPa as cracks close (Alm et al., 1985; Griffiths et al., 2018; Homand-Etienne & Houpert, 1989).

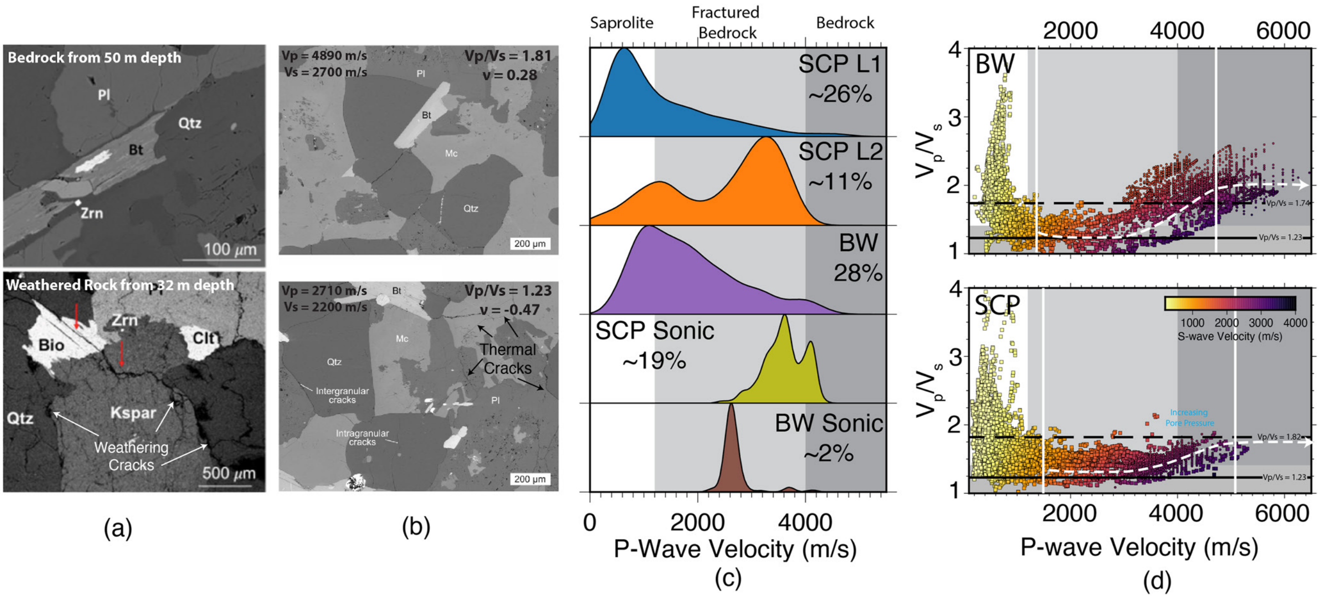

Figure 4. (a) SEM sections from a borehole ~3 km Southwest of our location (Holbrook et al., 2019). The top panel shows an unweathered bedrock sample from 50 m depth and the bottom shows a weathered bedrock from 32 m depth. (b) SEM sections from a thermally treated granite from Griffiths et al. (2018). The top is the untreated sample, and the bottom plot is an SEM section after being heat treated to 450 C to induce microcracks. The samples' V_p, V_s, V_p/V_s values, and Poisson's ratios are reported on the panels. (c) Probability density functions of V_p for all data with V_p/V_s values less than 1.4 ($\upsilon < 0$). The percentage data with values less than 1.4 are shown in each plot. Background colors are CZ structure based on V_p. White is saprolite ($V_p \leq 1{,}200$ m/s), gray is fractured bedrock ($1{,}200$ m/s $< V_p \leq 4{,}000$ m/s), and dark gray is unfractured bedrock ($V_p > 4{,}000$ m/s). (d) V_p/V_s values plotted as a function of V_p and colored by V_s. Gray shaded regions are the same as panel d with an additional gray rectangle to highlight V_p/V_s values less than 1.4. The top panel is for BW. The bottom panel is for SCP, which includes both SCP L1 and SCP L2. Squares are data from seismic refraction surveys, and circles are from sonic logs. The dashed black line is the theoretical V_p/V_s values assuming no porosity based on the mineralogic compositions from Flinchum et al. (2018a) and Flinchum et al. (2018b) for BW and Holbrook et al. (2019) for SCP (Supporting Information S1). The solid black line is the V_p/V_s value from the thermally treated granite shown in panel c. The dashed white line is our interpretation of the V_p/V_s value behavior as physical and chemical weathering creates porosity. The vertical white lines are approximate boundaries of change. The line at the highest P-wave velocities marks the onset of weathering, and the line around 1,200 m/s marks the location where V_p/V_s values increase.

We propose that a combination of low effective pressures in the CZ and biotite expansion can produce auxetic behavior similar to thermally cracked granites. Biotite expansion generates new fractures, providing more mineral surface area for geochemical reactions (Bazilevskaya et al., 2013; Buss et al., 2008; Tian et al., 2019) and sufficient energy density to fracture rock over cm length scales in granites (Goodfellow et al., 2016; Goodfellow & Hilley, 2022). The stresses created by biotite expansion can impact the state of stress on the hillslope scales (Shen et al., 2019; Xu et al., 2022). The low effective pressures in the CZ (<1 MPa) allow fractures created by biotite to remain open. Scanning electron microscope (SEM) sections show that weathering cracks resemble auxetic thermally cracked granite (Figures 4a and 4b) (Griffiths et al., 2018). The velocity changes caused by heat treatment are similar to the contrasts between unweathered and fractured bedrock in our survey, with initial granite velocities ($V_p = 4{,}890$ m/s; $V_s = 2{,}700$ m/s) showing more rapid reduction in V_p than V_s ($V_p = 2{,}710$ m/s; $V_s = 2{,}200$ m/s), producing an auxetic response (Figure 4a). The auxetic behavior is restricted to structures above bedrock ($V_p < 4{,}000$ m/s) (Figure 4c). Probability density functions (PDF) of all model parameters with V_p/V_s values less than 1.4 show that the probability is less than 3% when V_p is greater than 4,000 m/s (Figure 4c). The notable exception is the sonic velocities at SCP, where the probability is higher (20%). However, if the bedrock velocity at SCP is 4,500 m/s, the probability of auxetic behavior is reduced to zero (Figure 4d). Based on the mineralogy at SCP, the bedrock velocity should be 4,480 m/s (Table S3 in Supporting Information S1).

Our data suggest that the auxetic behavior extends into the saprolite ($V_p < 1{,}200$ m/s) (Figure 4c). This is possible because the saprolite retains the original fabric of the underlying bedrock (Dixon et al., 2009; Graham et al., 2010). The preserved fractures and fabrics in saprolite, even at depths less than a few meters, have caused seismic anisotropy (Eppinger et al., 2021; Novitsky et al., 2018). Furthermore, the volumetric strain of saprolite at seven crystalline rock sites has been associated with positive volumetric expansion (Riebe et al., 2021), which suggests an underlying physical weathering mechanism that creates additional porosity. We speculate that the fractures created by biotite expansion remain open in saprolite. We expect V_p/V_s values less than 1.4 will occur in locations with positive volumetric strains, like the hillslope in the Southern Sierras, where strains over hundreds of meters exceeded 100% (Hayes et al., 2019).

Finally, we expect a more rapid decrease in the V_p/V_s value for bedrock with higher biotite concentration, again consistent with our data. The SCP site is on a biotite gneiss with ∼4% biotite (Holbrook et al., 2019). In contrast, the BW site has ∼7.5% biotite (Edwards & Frost, 2000; Flinchum et al., 2018a; Frost et al., 1999). Similarly, previous work in the Southern Sierras showed that small differences in biotite concentration (2%–3%) can strongly impact CZ architecture (Callahan et al., 2022). Our data show a rapid decrease in the V_p/V_s value from bedrock to fractured rock (∼1.7 to ∼1.2) at BW (Figure 4d) but a smaller at SCP (Figure 4d), consistent with biotite cracking as an important mechanism of porosity creation (Figure 4d).

Our interpretation suggests that V_p is more sensitive to fracturing than V_s. This is illustrated in the thermally treated sample, which showed the auxetic behavior was created by a faster drop in V_p relative to V_s (Figure 4a). Our data required significant additional analysis because our V_s were suspiciously high. The V_p sensitivity is consistent with challenges associated with using existing rock physics models to estimate porosity in weathered and crystalline rocks at the BW site (Flinchum et al., 2018a). At BW, a porous media rock physics model had to be used for the saprolite (V_p < 1,200 m/s), and a differential effective medium (DEM) mode had to be used in the fractured bedrock (see Figure 2 from Flinchum et al., 2018a). Porous media models assume the matrix is supported by individual grains (Dvorkin et al., 1999; Dvorkin & Nur, 1996; Hashin & Shtrikman, 1963; Mindlin, 1949), while differential effective media (DEM) models a solid material with penny-shaped inclusions (Berryman et al., 2002). Both models show that velocity decreases with increasing porosity. However, the porous media model requires higher porosities to reduce the velocity than the DEM model (see Figure 2 in Flinchum et al., 2018a). In other words, the faster reduction of V_p in the fractured bedrock is consistent with differences between DEM and porous media models for the mineralogy at the BW site.

5.2. Anisotropy, Water Saturation and Scaling Effects

P-wave velocities collected in saprolite over weathering crystalline bedrock can be anisotropic due to aligned fracture fabric or inherited foliation at field scales (Eppinger et al., 2021; Leone et al., 2020; Novitsky et al., 2018). The impact of anisotropy on V_p/V_s has been shown in laboratory studies (Wang et al., 2012). Therefore, depending on fracturing and foliation, measuring V_p along a slow axis and V_s along a fast axis could produce the low V_p/V_s values we observe. SCP L1 has much lower V_p/V_s values than SCP L2 (Figures 3d and 2). While we cannot rule out anisotropy as a contributing factor, we note that explaining the consistently low V_p/V_s values across the landscape with anisotropy alone would require near-vertical foliation with rather fortuitous alignment of strike directions perpendicular to the direction of each seismic transect. The could be tested with future seismic surveys to measure V_p/V_s values as a function of azimuth (Eppinger et al., 2021; Leone et al., 2020).

Seismic refraction velocities are averages over large volumes as a function of seismic wavelength (Flinchum et al., 2022). Because V_s is slower than V_p, S-waves have smaller wavelengths and therefore better resolution. Travel time tomography does not account for this difference in wavelength, but we did apply the same regularization and inverted the data on the same mesh for V_p and V_s. The contrasting wavelengths will cause the P- and S-waves to travel along slightly different paths and might cause the inversion to place boundaries in slightly different locations. If resolution and inversion regularization were the underlying cause of the low V_p/V_s values, we would expect the low V_p/V_s values to be isolated along major boundaries in the V_p and V_s models, contrary to what is observed (Figure 2). Future work could use joint inversion to structurally couple the V_p and V_s models to reduce the ambiguity around major V_p and V_s boundaries.

The V_p/V_s response is sensitive to changes in saturation (Brantut & David, 2018; Hamada, 2004), since fluid-filled pores increase the bulk modulus and density of a porous material but not the shear modulus. This effect can be frequency-dependent (Biot, 1956a, 1956b), resulting in squirt flow (Markova et al., 2014). The V_p increase can be dramatic in unconsolidated sands, where V_p can rise rapidly from 100s of m/s to ∼1,500 m/s as full saturation is approached (Bachrach & Nur, 1998; Gregory, 1976; Liu & Zhao, 2015; Nur & Simmons, 1969). However, because water does not impact the shear modulus G, V_s decreases slightly with increasing saturation as density increases. This phenomenon is why V_p/V_s values have been used to map the water table (Flinchum et al., 2020; Grelle & Guadagno, 2009; Mota & Santos, 2010; Pasquet et al., 2015a). There isn't a clear increase in V_p/V_s value that would indicate the water table in our data (Figure 2).

More carefully planned experiments are required to rule out the impacts of anisotropy caused by fabric and foliation, the role of water saturation, and scaling effects. Low V_p/V_s values at two sites in two different climates, in both foliated and unfoliated bedrock, suggests a deeper underlying mechanism worth investigating. CZ geophysicists working in the low effective pressures near Earth's surface should remain open-minded to a much wider range of V_p/V_s values than usually expected at higher pressures because small cracks and fractures will remain open.

6. Conclusions

The results presented in this study show anomalously low V_p/V_s values from both seismic refraction and downhole sonic log data in weathered granites with different histories, lithologies, and climates. We argue that fractures generated by the expansion of biotite are a plausible mechanism to explain the low V_p/V_s values observed in the CZ. Observations that support our interpretation are that the low V_p/V_s values (<1.4) occur only in the fractured rock and saprolite, and that SEM images of an auxetic granite appear similar to weathered rock at our sites and have similar V_p, V_s, and V_p/V_s values to those observed in our data. Given the line configurations, we cannot rule out the impacts of seismic anisotropy, scaling, and water saturation. Nevertheless, in near-surface environments, the assumption that materials have a positive Poisson's ratio might not always be justified, especially weathered and fractured materials at low effective pressures.

Data Availability Statement

The data used for this manuscript can be found and downloaded on Hydroshare: Flinchum, B. A. (2023).

Acknowledgments
We are grateful to the many undergraduate researchers who helped collect the seismic refraction data for the Blair Wallis line as part of the Wyoming Center for Environmental Hydrology and Geophysics (WyCEHG) team. We are also grateful to the Bedrock Critical Zone Network team: Wynnie Avent, Alexa Dodson, Dillon Romero, Charles Lallatin, Kaycee Lallatin, Sky Bensel, Aran Lovato, Wade Renard, Annalee Chiaviello, and many others involved in logistics and project planning. This study was supported by the National Science Foundation award “Collaborative Research: Network Cluster: Bedrock controls on the deep critical zone, landscapes, and ecosystems” (NSFEAR 2012357, NSFEAR 2012227, NSFEAR 2012353) and “Water in a Changing West: The Wyoming Center for Environmental Hydrology and Geophysics” (NSFEPS 1208909).

References

Acuna, D., Gutiérrez, F., Silva, R., Palza, H., Nunez, A. S., & Düring, G. (2022). A three step recipe for designing auxetic materials on demand. *Communications Physics*, *5*(1), 113. https://doi.org/10.1038/s42005-022-00876-5

Alderson, A., & Alderson, K. L. (2007). Auxetic materials. *Proceedings of the Institution of Mechanical Engineers, Part G: Journal of Aerospace Engineering*, *221*(4), 565–575. https://doi.org/10.1243/09544100jaero185

Alm, O., Jaktlund, L.-L., & Shaoquan, K. (1985). The influence of microcrack density on the elastic and fracture mechanical properties of Stripa granite. *Physics of the Earth and Planetary Interiors*, *40*(3), 161–179. https://doi.org/10.1016/0031-9201(85)90127-x

Anderson, R. S., Rajaram, H., & Anderson, S. P. (2019). Climate driven coevolution of weathering profiles and hillslope topography generates dramatic differences in critical zone architecture. *Hydrological Processes*, *33*(1), 4–19. https://doi.org/10.1002/hyp.13307

Anderson, S. P., von Blanckenburg, F., & White, A. F. (2007). Physical and chemical controls on the critical zone. *Elements*, *3*(5), 315–319. https://doi.org/10.2113/gselements.3.5.315

Bachrach, R., & Nur, A. (1998). High-resolution shallow-seismic experiments in sand, Part I: Water table, fluid flow, and saturation. *Geophysics*, *63*(4), 1225–1233. https://doi.org/10.1190/1.1444423

Baughman, R. H. (2003). Auxetic materials: Avoiding the shrink. *Nature*, *425*(6959), 667. https://doi.org/10.1038/425667a

Bazilevskaya, E., Lebedeva, M., Pavich, M., Rother, G., Parkinson, D. Y., Cole, D., & Brantley, S. L. (2013). Where fast weathering creates thin regolith and slow weathering creates thick regolith. *Earth Surface Processes and Landforms*, *38*(8), 847–858. https://doi.org/10.1002/esp.3369

Befus, K. M., Sheehan, A. F., Leopold, M., Anderson, S. P., & Anderson, R. S. (2011). Seismic constraints on critical zone architecture, boulder creek watershed, Front Range, Colorado. *Vadose Zone Journal*, *10*(4), 1342. https://doi.org/10.2136/vzj2010.0108er

Berryman, J. G., Pride, S. R., & Wang, H. F. (2002). A differential scheme for elastic properties of rocks with dry or saturated cracks. *Geophysical Journal International*, *151*(2), 597–611. https://doi.org/10.1046/j.1365-246x.2002.01801.x

Biot, M. A. (1956a). Theory of propagation of elastic waves in a fluid-saturated porous solid. I. Low-frequency range. *Journal of the Acoustical Society of America*, *28*(2), 168–178. https://doi.org/10.1121/1.1908239

Biot, M. A. (1956b). Theory of propagation of elastic waves in a fluid-saturated porous solid. II. Higher frequency range. *Journal of the Acoustical Society of America*, *28*(2), 179–191. https://doi.org/10.1121/1.1908241

Brantley, S. L., McDowell, W. H., Dietrich, W. E., White, T. S., Kumar, P., Anderson, S. P., et al. (2017). Designing a network of critical zone observatories to explore the living skin of the terrestrial Earth. *Earth Surface Dynamics*, *5*(4), 841–860. https://doi.org/10.5194/esurf-5-841-2017

Brantut, N., & David, E. C. (2018). Influence of fluids on VP/VS ratio: Increase or decrease? *Geophysical Journal International*, *216*(3), 2037–2043. https://doi.org/10.1093/gji/ggy518

Buss, H. L., Lara, M. C., Moore, O. W., Kurtz, A. C., Schulz, M. S., & White, A. F. (2017). Lithological influences on contemporary and long-term regolith weathering at the Luquillo Critical Zone Observatory. *Geochimica et Cosmochimica Acta*, *196*, 224–251. https://doi.org/10.1016/j.gca.2016.09.038

Buss, H. L., Sak, P. B., Webb, S. M., & Brantley, S. L. (2008). Weathering of the Rio Blanco quartz diorite, Luquillo Mountains, Puerto Rico: Coupling oxidation, dissolution, and fracturing. *Geochimica et Cosmochimica Acta*, *72*(18), 4488–4507. https://doi.org/10.1016/j.gca.2008.06.020

Callahan, R. P., Riebe, C. S., Pasquet, S., Ferrier, K. L., Grana, D., Sklar, L. S., et al. (2020). Subsurface weathering revealed in hillslope-integrated porosity distributions. *Geophysical Research Letters*, *47*(15), e2020GL088322. https://doi.org/10.1029/2020gl088322

Callahan, R. P., Riebe, C. S., Sklar, L. S., Pasquet, S., Ferrier, K. L., Hahm, W. J., et al. (2022). Forest vulnerability to drought controlled by bedrock composition. *Nature Geoscience*, *15*(9), 714–719. https://doi.org/10.1038/s41561-022-01012-2

Chorover, J., Troch, P. A., Rasmussen, C., Brooks, P. D., Pelletier, J. D., Breshears, D. D., et al. (2011). How water, carbon, and energy drive critical zone evolution: The Jemez–Santa Catalina critical zone observatory. *Vadose Zone Journal*, *10*(3), 884–899. https://doi.org/10.2136/vzj2010.0132

Dixon, J. L., Heimsath, A. M., & Amundson, R. (2009). The critical role of climate and saprolite weathering in landscape evolution. *Earth Surface Processes and Landforms*, *34*(11), 1507–1521. https://doi.org/10.1002/esp.1836

Donaldson, A. M., Zimmer, M., Huang, M.-H., Johnson, K. N., Hudson-Rasmussen, B., Finnegan, N., et al. (2023). Symmetry in hillslope steepness and saprolite thickness between hillslopes with opposing aspects. *Journal of Geophysical Research: Earth Surface*, *128*(7), e2023JF007076. https://doi.org/10.1029/2023jf007076

Dvorkin, J., & Nur, A. (1996). Elasticity of high-porosity sandstones; theory for two North Sea data sets. *Geophysics*, *61*(5), 1363–1370. https://doi.org/10.1190/1.1444059

Dvorkin, J., Prasad, M., Sakai, A., & Lavoie, D. (1999). Elasticity of marine sediments: Rock physics modeling. *Geophysical Research Letters*, *26*(12), 1781–1784. https://doi.org/10.1029/1999gl900332

Edwards, B. R., & Frost, C. D. (2000). An overview of the petrology and geochemistry of the Sherman batholith, southeastern Wyoming Identifying multiple sources of Mesoproterozoic magmatism. *Rocky Mountain Geology*, *35*(1), 113–137. https://doi.org/10.2113/35.1.113

Eggler, D. H., Larson, E. E., & Bradley, W. C. (1969). Granites Grusses and Sherman Erosion surface southern Laramie Range Colorado-Wyoming. *American Journal of Science*, *267*(4), 510–522. https://doi.org/10.2475/ajs.267.4.510

Eppinger, B. J., Hayes, J. L., Carr, B. J., Moon, S., Cosans, C. L., Holbrook, W. S., et al. (2021). Quantifying depth-dependent seismic anisotropy in the critical zone enhanced by weathering of a piedmont schist. *Journal of Geophysical Research: Earth Surface*, *126*(10), e2021JF006289. https://doi.org/10.1029/2021jf006289

Evans, K. E., & Alderson, K. L. (2000). Auxetic materials: The positive side of being negative. *Engineering Science & Education Journal*, *9*(4), 148–154. https://doi.org/10.1049/esej:20000402

Flinchum, B. A. (2023). Supporting data repository for paper for negative Poisson ratios determined from Vp/Vs values are a possible indicator for microcracks in the critical zone, HydroShare [Dataset]. HydroShare. http://www.hydroshare.org/resource/cc5c632344bf44c4a082311ac8c6050a

Flinchum, B. A., Banks, E., Hatch, M., Batelaan, O., Peeters, L., & Pasquet, S. (2020). Identifying recharge under subtle ephemeral features in flat-lying semi-arid region using a combined geophysical approach. *Hydrology and Earth System Sciences Discussions*, *2020*, 1–31. https://doi.org/10.5194/hess-2019-576

Flinchum, B. A., Holbrook, W. S., & Carr, B. J. (2022). What do P-wave velocities tell us about the critical zone? *Frontiers in Water*, *3*, 772185. https://doi.org/10.3389/frwa.2021.772185

Flinchum, B. A., Holbrook, W. S., Grana, D., Parsekian, A. D., Carr, B. J., Hayes, J. L., & Jiao, J. (2018a). Estimating the water holding capacity of the critical zone using near-surface geophysics. *Hydrological Processes*, *32*(22), 3308–3326. https://doi.org/10.1002/hyp.13260

Flinchum, B. A., Holbrook, W. S., Parsekian, A. D., & Carr, B. J. (2019). Characterizing the critical zone using borehole and surface nuclear magnetic resonance. *Vadose Zone Journal*, *18*, 1–18. https://doi.org/10.2136/vzj2018.12.0209

Flinchum, B. A., Holbrook, W. S., Rempe, D., Moon, S., Riebe, C. S., Carr, B. J., et al. (2018b). Critical zone structure under a granite ridge inferred from drilling and three-dimensional seismic refraction data. *Journal of Geophysical Research: Earth Surface*, *123*(6), 1317–1343. https://doi.org/10.1029/2017jf004280

Frost, C. D., Frost, B. R., Chamberlain, K. R., & Edwards, B. R. (1999). Petrogenesis of the 1.43 Ga Sherman Batholith, SE Wyoming, USA: A reduced, Rapakivi-type Anorogenic Granite. *Journal of Petrology*, *40*(12), 1771–1802. https://doi.org/10.1093/petroj/40.12.1771

Gercek, H. (2007). Poisson's ratio values for rocks. *International Journal of Rock Mechanics and Mining Sciences*, *44*, 1–13. https://doi.org/10.1016/j.ijrmms.2006.04.011

Goodfellow, B. W., & Hilley, G. E. (2022). Climatic and lithological controls on the structure and thickness of granitic weathering zones. *Earth and Planetary Science Letters*, *600*, 117890. https://doi.org/10.1016/j.epsl.2022.117890

Goodfellow, B. W., Hilley, G. E., & Schulz, M. S. (2011). Vadose zone controls on weathering intensity and depth: Observations from Grussic Saprolites. *Applied Geochemistry*, *26*, S36–S39. https://doi.org/10.1016/j.apgeochem.2011.03.023

Goodfellow, B. W., Hilley, G. E., Webb, S. M., Sklar, L. S., Moon, S., & Olson, C. A. (2016). The chemical, mechanical, and hydrological evolution of weathering granitoid. *Journal of Geophysical Research: Earth Surface*, *121*(8), 1410–1435. https://doi.org/10.1002/2016jf003822

Graham, R., Rossi, A., & Hubbert, R. (2010). Rock to regolith conversion: Producing hospitable substrates for terrestrial ecosystems. *Geological Society of America Today*, *20*, 4–9. https://doi.org/10.1130/gsat57a.1

Greaves, G. N., Greer, A. L., Lakes, R. S., & Rouxel, T. (2011). Poisson's ratio and modern materials. *Nature Materials*, *10*(11), 823–837. https://doi.org/10.1038/nmat3134

Gregory, A. R. (1976). Fluid saturation effects on dynamic elastic properties of sedimentary rocks. *Geophysics*, *41*(5), 895–921. https://doi.org/10.1190/1.1440671

Grelle, G., & Guadagno, F. M. (2009). Seismic refraction methodology for groundwater level determination: "Water seismic index.". *Journal of Applied Geophysics*, *68*(3), 301–320. https://doi.org/10.1016/j.jappgeo.2009.02.001

Griffiths, L., Lengliné, O., Heap, M. J., Baud, P., & Schmittbuhl, J. (2018). Thermal cracking in westerly granite monitored using direct wave velocity, coda wave interferometry, and acoustic emissions. *Journal of Geophysical Research: Solid Earth*, *123*(3), 2246–2261. https://doi.org/10.1002/2017jb015191

Haldorsen, J., Johnson, D. L., Plona, T., Sinha, B., Valero, H.-P., & Winkler, K. (2006). Borehole acoustic waves. *Oilfield Review*, *18*.

Hamada, G. M. (2004). Reservoir fluids identification using Vp/Vs ratio? *Oil and Gas Science and Technology*, *59*(6), 649–654. https://doi.org/10.2516/ogst:2004046

Hashin, Z., & Shtrikman, S. (1963). A variational approach to the theory of the elastic behaviour of multiphase materials. *Journal of the Mechanics and Physics of Solids*, *11*(2), 127–140. https://doi.org/10.1016/0022-5096(63)90060-7

Hayes, J. L., Riebe, C. S., Holbrook, W. S., Flinchum, B. A., & Hartsough, P. C. (2019). Porosity production in weathered rock: Where volumetric strain dominates over chemical mass loss. *Science Advances*, *5*(9), eaao0834. https://doi.org/10.1126/sciadv.aao0834

Hill, R. (1963). Elastic properties of reinforced solids: Some theoretical principles. *Journal of the Mechanics and Physics of Solids*, *11*(5), 357–372. https://doi.org/10.1016/0022-5096(63)90036-x

Holbrook, W. S., Marcon, V., Bacon, A. R., Brantley, S. L., Carr, B. J., Flinchum, B. A., et al. (2019). Links between physical and chemical weathering inferred from a 65-m-deep borehole through Earth's critical zone. *Scientific Reports*, *9*(1), 4495. https://doi.org/10.1038/s41598-019-40819-9

Holbrook, W. S., Riebe, C. S., Elwaseif, M., Hayes, J. L., Basler-Reeder, K., Harry, D. L., et al. (2014). Geophysical constraints on deep weathering and water storage potential in the Southern Sierra Critical Zone Observatory. *Earth Surface Processes and Landforms*, *39*(3), 366–380. https://doi.org/10.1002/esp.3502

Homand-Etienne, F., & Houpert, R. (1989). Thermally induced microcracking in granites: Characterization and analysis. *International Journal of Rock Mechanics and Mining Sciences & Geomechanics Abstracts*, *26*(2), 125–134. https://doi.org/10.1016/0148-9062(89)90001-6

Hornby, B. E., & Murphy, W. F. (1987). V p/V s in unconsolidated oil sands; shear from Stoneley. *Geophysics*, *52*(4), 502–513. https://doi.org/10.1190/1.1442320

Hunter, J. A., Crow, H. L., Stephenson, W. J., Pugin, A. J.-M., Williams, R. A., Harris, J. B., et al. (2022). Seismic site characterization with shear wave (SH) reflection and refraction methods. *Journal of Seismology*, *26*(4), 631–652. https://doi.org/10.1007/s10950-021-10042-z

Ji, S., Li, L., Motra, H. B., Wuttke, F., Sun, S., Michibayashi, K., & Salisbury, M. H. (2018). Poisson's ratio and auxetic properties of natural rocks. *Journal of Geophysical Research: Solid Earth*, *123*(2), 1161–1185. https://doi.org/10.1002/2017jb014606

Ji, S., Wang, Q., & Li, L. (2019). Seismic velocities, Poisson's ratios and potential auxetic behavior of volcanic rocks. *Tectonophysics*, *766*, 270–282. https://doi.org/10.1016/j.tecto.2019.06.013

Juhlin, C. (1995). Finite-difference elastic wave propagation in 2D heterogeneous transversely isotropic media1. *Geophysical Prospecting*, *43*(6), 843–858. https://doi.org/10.1111/j.1365-2478.1995.tb00284.x

Keifer, I., Dueker, K., & Chen, P. (2019). Ambient Rayleigh wave field imaging of the critical zone in a weathered granite terrane. *Earth and Planetary Science Letters*, *510*, 198–208. https://doi.org/10.1016/j.epsl.2019.01.015

Klos, P. Z., Goulden, M. L., Riebe, C. S., Tague, C. L., O'Geen, A. T., Flinchum, B. A., et al. (2018). Subsurface plant-accessible water in mountain ecosystems with a Mediterranean climate. *Wiley Interdisciplinary Reviews: Water*, *5*(3), e1277. https://doi.org/10.1002/wat2.1277

Lebedeva, M. I., & Brantley, S. L. (2017). Weathering and erosion of fractured bedrock systems. *Earth Surface Processes and Landforms*, *42*(13), 2090–2108. https://doi.org/10.1002/esp.4177

Lebedeva, M. I., & Brantley, S. L. (2023). Using homogenized models to explore the effect of fracture densities on weathering. *American Journal of Science*, *323*. https://doi.org/10.2475/001c.68308

Leone, J. D., Holbrook, W. S., Riebe, C. S., Chorover, J., Ferré, T. P. A., Carr, B. J., & Callahan, R. P. (2020). Strong slope-aspect control of regolith thickness by bedrock foliation. *Earth Surface Processes and Landforms*, *45*(12), 2998–3010. https://doi.org/10.1002/esp.4947

Li, L., & Ji, S. (2021). A new interpretation for formation of orthogonal joints in quartz sandstone. *Journal of Rock Mechanics and Geotechnical Engineering*, *13*(2), 289–299. https://doi.org/10.1016/j.jrmge.2020.08.003

Liberty, L. M., Yelton, J., Skurtveit, E., Braathen, A., Midtkandal, I., & Evans, J. P. (2022). Regolith and host rock influences on CO2 leakage: Active source seismic profiling across the Little Grand Wash fault, Utah. *International Journal of Greenhouse Gas Control*, *119*, 103742. https://doi.org/10.1016/j.ijggc.2022.103742

Liu, X., Zhu, T., & Hayes, J. (2022). Critical zone structure by elastic full waveform inversion of seismic refractions in a sandstone catchment, Central Pennsylvania, USA. *Journal of Geophysical Research: Solid Earth*, *127*(3), e2021JB023321. https://doi.org/10.1029/2021jb023321

Liu, Z., & Zhao, J. (2015). An experimental study of velocity-saturation relationships in volcanic rocks. *The Open Petroleum Engineering Journal*, *8*(1), 142–152. https://doi.org/10.2174/1874834101508010142

Markova, I., Jarillo, G. R., Markov, M., & Gurevich, B. (2014). Squirt flow influence on sonic log parameters. *Geophysical Journal International*, *196*(2), 1082–1091. https://doi.org/10.1093/gji/ggt442

Mavko, G., Mukerji, T., & Dvorkin, J. (2009). The rock physics handbook (pp. 21–80). https://doi.org/10.1017/cbo9780511626753.003

Mi, B., Xia, J., & Xu, Y. (2015). Finite-difference modeling of SH-wave conversions in shallow shear-wave refraction surveying. *Journal of Applied Geophysics*, *119*, 71–78. https://doi.org/10.1016/j.jappgeo.2015.05.009

Mindlin, R. D. (1949). Compliance of elastic bodies in contact. *Journal of Applied Mechanics*, *16*(3), 259–268. https://doi.org/10.1115/1.4009973

Molnar, P., Anderson, R. S., & Anderson, S. P. (2007). Tectonics, fracturing of rock, and erosion. *Journal of Geophysical Research*, *112*(F3), F03014. https://doi.org/10.1029/2005jf000433

Moser, T. (1991). Shortest-path calculation of seismic rays. *Geophysics*, *56*(1), 59–67. https://doi.org/10.1190/1.1442958

Mota, R., & Santos, F. A. M. (2010). 2D sections of porosity and water saturation from integrated resistivity and seismic surveys. *Near Surface Geophysics*, *8*(6), 575–584. https://doi.org/10.3997/1873-0604.2010042

Novitsky, C. G., Holbrook, W. S., Carr, B. J., Pasquet, S., Okaya, D., & Flinchum, B. A. (2018). Mapping inherited fractures in the critical zone using seismic anisotropy from circular surveys. *Geophysical Research Letters*, *45*(7), 3126–3135. https://doi.org/10.1002/2017gl075976

Nur, A., & Simmons, G. (1969). The effect of saturation on velocity in low porosity rocks. *Earth and Planetary Science Letters*, *7*(2), 183–193. https://doi.org/10.1016/0012-821x(69)90035-1

Park, C. B., Miller, R. D., & Xia, J. (1999). Multichannel analysis of surface waves. *Geophysics*, *64*(3), 800–808. https://doi.org/10.1190/1.1444590

Pasquet, S., Bodet, L., Dhemaied, A., Mouhri, A., Vitale, Q., Rejiba, F., et al. (2015a). Detecting different water table levels in a shallow aquifer with combined P-surface and SH-wave surveys: Insights from VP/VS or Poisson's ratios. *Journal of Applied Geophysics*, *113*, 38–50. https://doi.org/10.1016/j.jappgeo.2014.12.005

Pasquet, S., Bodet, L., Longuevergne, L., Dhemaied, A., Camerlynck, C., Rejiba, F., & Guérin, R. (2015b). 2D characterization of near-surface: Surface-wave dispersion inversion versus refraction tomography. *Near Surface Geophysics*, *13*(4), 315–332. https://doi.org/10.3997/1873-0604.2015028

Pasquet, S., Holbrook, W. S., Carr, B. J., & Sims, K. W. W. (2016). Geophysical imaging of shallow degassing in a Yellowstone hydrothermal system. *Geophysical Research Letters*, *43*(23), 12027–12035. https://doi.org/10.1002/2016gl071306

Pavich, M. J. (1989). Regolith residence time and the concept of surface age of the Piedmont "Peneplain.". *Geomorphology*, *2*(1–3), 181–196. https://doi.org/10.1016/0169-555x(89)90011-1

Potyondy, D. O., & Cundall, P. A. (2004). A bonded-particle model for rock. *International Journal of Rock Mechanics and Mining Sciences*, *41*(8), 1329–1364. https://doi.org/10.1016/j.ijrmms.2004.09.011

Prasad, M. (2002). Acoustic measurements in unconsolidated sands at low effective pressure and overpressure detectionOverpressure Detection in Sands. *Geophysics*, *67*(2), 405–412. https://doi.org/10.1190/1.1468600

Rempe, D. M., & Dietrich, W. E. (2014). A bottom-up control on fresh-bedrock topography under landscapes. *Proceedings of the National Academy of Sciences of the United States of America*, *111*(18), 6576–6581. https://doi.org/10.1073/pnas.1404763111

Ren, S., Parsekian, A. D., Zhang, Y., & Carr, B. J. (2019). Hydraulic conductivity calibration of logging NMR in a granite aquifer, Laramie Range, Wyoming. *Groundwater*, *57*(2), 303–319. https://doi.org/10.1111/gwat.12798

de Richter, D. B., & Mobley, M. L. (2009). Monitoring Earth's critical zone. *Science*, *326*(5956), 1067–1068. https://doi.org/10.1126/science.1179117

Riebe, C. S., Callahan, R. P., Granke, S. B.-M., Carr, B. J., Hayes, J. L., Schell, M. S., & Sklar, L. S. (2021). Anisovolumetric weathering in granitic saprolite controlled by climate and erosion rate. *Geology*, *49*(5), 551–555. https://doi.org/10.1130/g48191.1

Rücker, C., Günther, T., & Wagner, F. M. (2017). pyGIMLi: An open-source library for modelling and inversion in geophysics. *Computers & Geosciences*, *109*, 106–123. https://doi.org/10.1016/j.cageo.2017.07.011

Salas-Romero, S., Malehmir, A., Snowball, I., & Brodic, B. (2021). Geotechnical site characterization using multichannel analysis of surface waves: A case study of an area prone to quick-clay landslides in southwest Sweden. *Near Surface Geophysics*, *19*(6), 699–715. https://doi.org/10.1002/nsg.12173

Salem, H. S. (2015). Poisson's ratio and the porosity of surface soils and shallow sediments, determined from seismic compressional and shear wave velocities. *Géotechnique*, *50*(4), 461–463. https://doi.org/10.1680/geot.2000.50.4.461

Secor, D. T., Snoke, A. W., Bramlett, K. W., Costello, O. P., & Kimbrell, O. P. (1986). Character of the Alleghanian orogeny in the southern Appalachians: Part I. Alleghanian deformation in the eastern piedmont of South Carolina. *GSA Bulletin*, *97*(11), 1319–1328. https://doi.org/10.1130/0016-7606(1986)97<1319:cotaoi>2.0.co;2

Shen, X., Arson, C., Ferrier, K. L., West, N., & Dai, S. (2019). Mineral weathering and bedrock weakening: Modeling microscale bedrock damage under biotite weathering. *Journal of Geophysical Research: Earth Surface*, *124*(11), 2623–2646. https://doi.org/10.1029/2019jf005068

Sherwood, W. C., Hartshorn, T., & Eaton, L. S. (2010). Soils, geomorphology, landscape evolution, and land use in the Virginia Piedmont and Blue Ridge.

St Clair, J., Moon, S., Holbrook, W. S., Perron, J. T., Riebe, C. S., Martel, S. J., et al. (2015). Geophysical imaging reveals topographic stress control of bedrock weathering. *Science*, *350*(6260), 534–538. https://doi.org/10.1126/science.aab2210

Stein, S., & Wysession, M. (2003). *An introduction to seismology earthquakes, and Earth structure*. Blackwell Publishing Ltd.

Stockwell, J. W. (1999). The CWP/SU: Seismic Un∗x package11The SU project is partially supported by CWP's consortium project on seismic inverse methods for complex structures, the SEG foundation and the gas research institute. *Computers & Geosciences*, *25*(4), 415–419. https://doi.org/10.1016/s0098-3004(98)00145-9

Stümpel, H., Kähler, S., Meissner, R., & Milkereit, B. (1984). The use of seismic shear waves and compressional waves for lithological problems of shallow sediments. *Geophysical Prospecting*, *32*(4), 662–675. https://doi.org/10.1111/j.1365-2478.1984.tb01712.x

Tian, Z., Hartsough, P. C., & O'Geen, A. T. (2019). Lithologic, climatic and depth controls on critical zone transformations. *Soil Science Society of America Journal*, *83*(2), 437–447. https://doi.org/10.2136/sssaj2018.03.0120

Trichandi, R., Bauer, K., Ryberg, T., Scherler, D., Bataille, K., & Krawczyk, C. M. (2022). Combined seismic and borehole investigation of the deep granite weathering structure—Santa Gracia Reserve case in Chile. *Earth Surface Processes and Landforms*, *47*(14), 3302–3316. https://doi.org/10.1002/esp.5457

Uecker, R. K., Flinchum, B. A., Holbrook, W. S., & Carr, B. J. (2023). Mapping bedrock topography: A seismic refraction survey and landscape analysis in the Laramie Range, Wyoming. *Frontiers in Water*, *5*, 1057725. https://doi.org/10.3389/frwa.2023.1057725

Uhlemann, S., Hagedorn, S., Dashwood, B., Maurer, H., Gunn, D., Dijkstra, T., & Chambers, J. (2016). Landslide characterization using P- and S-wave seismic refraction tomography—The importance of elastic moduli. *Journal of Applied Geophysics*, *134*, 64–76. https://doi.org/10.1016/j.jappgeo.2016.08.014

Wang, W., Chen, P., Keifer, I., Dueker, K., Lee, E.-J., Mu, D., et al. (2019). Weathering front under a granite ridge revealed through full-3D seismic ambient-noise tomography. *Earth and Planetary Science Letters*, *509*, 66–77. https://doi.org/10.1016/j.epsl.2018.12.038

Wang, X.-Q., Schubnel, A., Fortin, J., David, E. C., Guéguen, Y., & Ge, H.-K. (2012). High Vp/Vs ratio: Saturated cracks or anisotropy effects? *Geophysical Research Letters*, *39*(11), L11307. https://doi.org/10.1029/2012gl051742

Xia, J., Miller, R. D., & Park, C. B. (1999). Estimation of near-surface shear-wave velocity by inversion of Rayleigh waves. *Geophysics*, *64*(3), 691–700. https://doi.org/10.1190/1.1444578

Xu, T., Shen, X., Reed, M., West, N., Ferrier, K. L., & Arson, C. (2022). Anisotropy and microcrack propagation induced by weathering, regional stresses and topographic stresses. *Journal of Geophysical Research: Solid Earth*, *127*(7), e2022JB024518. https://doi.org/10.1029/2022jb024518

Zaitsev, V. Y., Radostin, A. V., Pasternak, E., & Dyskin, A. (2017a). Extracting real-crack properties from non-linear elastic behaviour of rocks: Abundance of cracks with dominating normal compliance and rocks with negative Poisson ratios. *Nonlinear Processes in Geophysics*, *24*(3), 543–551. https://doi.org/10.5194/npg-24-543-2017

Zaitsev, V. Y., Radostin, A. V., Pasternak, E., & Dyskin, A. (2017b). Extracting shear and normal compliances of crack-like defects from pressure dependences of elastic-wave velocities. *International Journal of Rock Mechanics and Mining Sciences*, *97*, 122–133. https://doi.org/10.1016/j.ijrmms.2017.04.009

Zhao, Z. (2016). Thermal influence on mechanical properties of granite: A microcracking perspective. *Rock Mechanics and Rock Engineering*, *49*(3), 747–762. https://doi.org/10.1007/s00603-015-0767-1

Zhao, Z., Xu, H., Wang, J., Zhao, X., Cai, M., & Yang, Q. (2020). Auxetic behavior of Beishan granite after thermal treatment: A microcracking perspective. *Engineering Fracture Mechanics*, *231*, 107017. https://doi.org/10.1016/j.engfracmech.2020.107017

Zimmer, M., Prasad, M., & Mavko, G. (2002). Pressure and porosity influences on VP-VS ratio in unconsolidated sands. *The Leading Edge*, *21*(2), 178–183. https://doi.org/10.1190/1.1452609

Zisman, W. A. (1933). Comparison of the statically and seismologically determined elastic constants of rocks. *Proceedings of the National Academy of Sciences of the United States of America*, *19*(7), 680–686. https://doi.org/10.1073/pnas.19.7.680